Diffeomorphic Registration for Retinotopic Maps of Multiple Visual Regions

Yanshuai Tu
Arizona State University - Tempe Campus: Arizona State University
Zhong-Lin Lu
New York University
Yalin Wang (ylwang@asu.edu)
Arizona State University https://orcid.org/0000-0002-6241-735X

Research Article

Keywords: Retinotopic map, fMRI analysis, Diffeomorphic Registration, Beltrami Coefficient, Landmarks.

Posted Date: June 4th, 2021

DOI: https://doi.org/10.21203/rs.3.rs-582560/v1

Version of Record: A version of this preprint was published at Brain Structure and Function on March 24th, 2022. See the published version at https://doi.org/10.1007/s00429-022-02480-3.

Diffeomorphic Registration for Retinotopic Maps of Multiple Visual Regions

Yanshuai Tu MS[1] [0000-0002-4619-2613], Zhong-Lin Lu PhD[2, 3, 4] [0000-0002-7295-727X], Yalin Wang PhD[1] [0000-0002-6241-735X]

[1]School of Computing, Informatics, and Decision Systems Engineering, Arizona State University, Tempe, AZ, USA

[2] Division of Arts and Sciences, New York University Shanghai, Shanghai, China,

[3] Center for Neural Science and Department of Psychology, New York University, New York, United States of America,

[4] NYU-ECNU Institute of Brain and Cognitive Science, NYU Shanghai, Shanghai, China

To be submitted to *special Issue on "Structure and Function of the Visual System," of Brain Structure and Function*

[*]Please send correspondence to:

E-mail: *zhonglin@nyu.edu or ylwang@asu.edu*

ABSTRACT

Retinotopic map, the mapping between visual inputs on the retina and neuronal responses on cortical surface, is one of the central topics in vision science. Typically, human retinotopic maps are constructed by analyzing functional magnetic resonance responses to designed visual stimuli on cortical surface. Although it is widely used in visual neuroscience, retinotopic maps are limited by measurement noise and resolution. One promising approach to improve the quality of retinotopic maps is to register individual subject's retinotopic maps to a retinotopic template or atlas. However, none of the existing retinotopic registration methods has explicitly quantified the diffeomorphic condition, that is, retinotopic maps can be aligned by stretching/compressing but without tearing up. Here, we developed *Diffeomorphic Registration for Retinotopic Maps (DRRM)* to simultaneously align retinotopic maps in multiple visual regions under the diffeomorphic condition. Specifically, we used the Beltrami coefficient to model the diffeomorphic condition and performed surface registration based on retinotopic coordinates. The overall framework is simple and elegant and preserves topological condition defined in the atlas. We further developed a unique performance evaluation protocol and compared the performance of the new method with several existing image intensity-based registration methods on both synthetic and real datasets. The results showed that DRRM is superior to the existing methods in achieving diffeomorphic mappings in synthetic and empirical data from 3T and 7T magnets. DRRM may improve the interpretation of low-quality retinotopic maps and facilitate adoption of retinotopic maps in clinical settings.

Keywords: Retinotopic map, fMRI analysis, Diffeomorphic Registration, Beltrami Coefficient, Landmarks.

DECLARATIONS

Funding

Y. T. and Y. W. were supported by DMS-1413417, RF1AG051710, R01EB025032, and R21AG065942; Z. L. was supported by DMS-1413417. The funders had no role in study design, data collection, analysis, manuscript preparation, or decision to publish.

Conflicts of interest/Competing interests

Y. T., Z. L., and Y. W. have a joint patent application, "Tu, Y., Y. Wang, and Z.-L. Lu, Methods and Systems for Precise Quantification of Human Sensory Cortical Areas," U.S. Patent Application No. 63/004. 2020.

Ethics approval (include appropriate approvals or waivers)

All the data we used are from the Human Connectome Project (HCP) and Study-Forrest dataset. We strictly followed their policy and rules in our analyses and presentation. There are no physical experiments associated with the study.

Consent to Participate and Consent for publication

All the authors listed above participated in the work either in the study stage or manuscript preparation, and are consent for publication.

Data and Code transparency

We developed custom code for the analysis. The executable code, intermediate results, figures, and screenshots are available on the OSF website https://osf.io/s25pe/.

Authors' contributions

Yanshuai Tu: Methodology, Conceptualization, Software, Original Draft Preparation.

Zhong-Lin Lu: Methodology, Supervision, Review & Editing.

Yalin Wang: Methodology, Supervision, Review & Editing, Project Administration, Funding.

1. INTRODUCTION

The human visual cortex is divided into multiple functional areas (Zeki and Shipp 1988), with most of them organized as retinotopic maps, that is, nearby neurons have receptive fields at nearby locations on the retina (Hubel and Wiesel 1962). Functional magnetic resonance imaging (fMRI) has provided a non-invasive way to measure cortical activations to carefully designed visual stimuli and enabled construction of retinotopic maps based on the populational receptive field (pRF) model (Warnking et al. 2002; Dumoulin and Wandell 2008). Features from the retinotopic maps have been used to study cortical plasticity (Wandell and Smirnakis 2009), cortical development (Conner et al. 2004), and brain simulations (Swindale 2000), among many other applications.

Unfortunately, the low signal-noise ratio (*SNR*) and spatial resolution of fMRI (Vasseur et al. 2010) has limited the quality of the decoded retinotopic maps (Warnking et al. 2002; Li et al. 2007), especially when the organization is more complicated (Wandell and Winawer 2011). Although post-smoothing, e.g., (Qiu et al. 2006b, a) is applicable, it is challenging to achieve a significant improvement. As a result, it is difficult to reach reliable conclusions based on retinotopic maps of a single subject, and group-level analysis is necessary.

A critical step in group-level retinotopic map analyses is surface co-registration of retinotopic maps from multiple subjects, which is quite challenging (Benson and Winawer 2018) because the cortical surface is convoluted and individual retinotopic maps are noisy. A number of sophisticated cortical surface registration packages, such as Freesurfer (Fischl and et al. 1999) and Brainsuit (Shattuck and Leahy 2002, Joshi et al. 2007) have been developed for *diffeomorphic* (i.e., invertible, differentiable) cortical surface alignment based on anatomical features (e.g., curvature, thickness) but not retinotopic data. Using structurally aligned cortical surfaces to align the corresponding retinotopic maps is not a viable option because retinotopic maps may misalign with the anatomical surfaces. Recently, multimodal registration (e.g., Multimodal Surface Matching; (Robinson et al. 2014)), based on fMRI time series, cortical surface and other features, has been developed to improve surface registration. It has however only incorporated fMRI time series but not the retinotopic coordinates associated with them and cannot be used for co-registration of retinotopic maps. Benson and colleagues (Benson et al. 2014; Benson and Winawer 2018) used retinotopic coordinates to register retinotopic maps by adopting a spring-damp-mass philosophy, together with several well-potentials and constraints to help the alignment and avoid over-stretching or over-compression. Although very intuitive and useful, the formulation did not explicitly consider the diffeomorphic condition, that is, retinotopic maps can be aligned by stretching/compressing but without tearing up, a property assumed in all brain surface registration works (Fischl and et al. 1999; Shattuck and Leahy 2002; Yeo et al. 2010). As a result, it introduced redundant constraints.

We developed *Diffeomorphic Registration for Retinotopic Map (DRRM) to* align retinotopic maps in multiple visual areas under the diffeomorphic condition. Diffeomorphic registration is a feasible way to ensure the topological condition in retinotopic mapping (Tu et al. 2020b): nearby neurons have receptive fields at nearby locations on the retina (Wandell et al. 2007). The raw pRF results cannot ensure such condition. Aligning a subject's retinotopic map to a topological template would make the post-registration retinotopic topological. In addition, diffeomorphic registration can be used to automatically infer the boundaries of the visual areas, avoiding tedious and error-prone manual labeling. Moreover, because the diffeomorphic condition is the natural requirement of surface registration without tearing, it is possible to delineate visual areas after a proper registration (Glasser et al. 2016).

We used the Beltrami coefficient (Gardiner and Lakic 2000) to model the diffeomorphic condition and performed surface registration based on retinotopic coordinates. Specifically, we modeled the

registration problem as an alignment optimization with diffeomorphic constraint, and proposed an iterative scheme to solve the registration model efficiently. Each iteration used simple demons (Thirion 1998) to improve registration accuracy, and processed the Beltrami coefficients of the registration function to ensure the diffeomorphic condition. Compared with Benson and Winawer (2018), we reduced the number of constraints and ensured the diffeomorphic condition during registration. As a significant extension of our previous conference paper (Tu et al. 2020a), the current work successfully applied the method to multiple datasets, including a low-quality retinotopy dataset, evaluated its performance with goodness of fit to fMRI time series instead of feature differences, and adopted a state-of-the-art atlas (Benson and Winawer 2018) instead of the average retinotopic maps as the template, which ensured the post-registration retinotopic maps satisfied the topological condition (Tu et al. 2020b).

2. METHODS

Fig. 1 illustrates the retinotopic map data collection and the proposed diffeomorphic registration process. The experiment collects structural MRI images (**Fig.** 1c) and multiple fMRI volumes at many time points (**Fig.** 1d) during visual stimulation (**Fig.** 1ab) for each subject. After a pre-processing of raw fMRI, the processed fMRI data (**Fig.** 1e) are projected back to cortical surface (**Fig.** 1f). The population receptive field analysis (pRF) (Dumoulin and Wandell 2008; Kay et al. 2013) is used to generate retinotopic map for a single subject (**Fig.** 1 g). The proposed diffeomorphic registration method registers an atlas to the raw retinotopic map data (**Fig.** 1h) and obtains registered retinotopic map (**Fig.** 1i), which is ready for further analyses.

In this section, the raw retinotopic map computation procedure is described in **Sec. 2.1**. The proposed multiple visual region registration algorithm is described in **Sec. 2.2**. We briefly describe our experimental data and atlas in **Sec. 2.3**. Registration performance metrics and comparison methods are reported in **Sec. 2.4**.

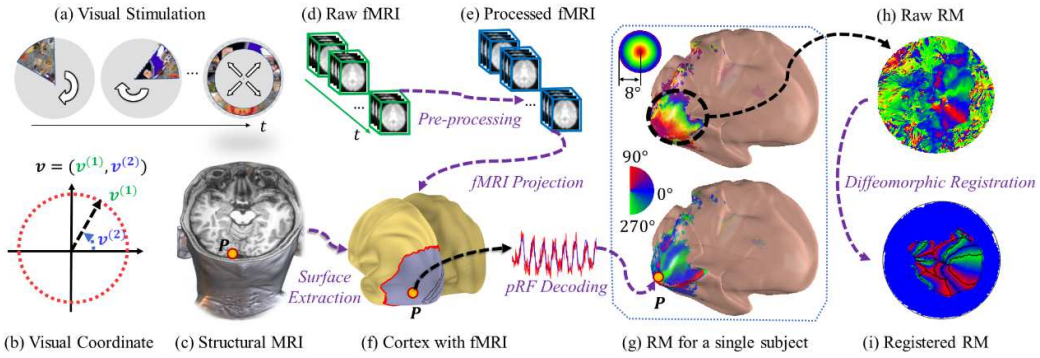

Figure 1. Illustration of a retinotopy experiment and the registration process: (a) visual stimuli, (b) the visual coordinate system, (c) structural MRI, (d) raw fMRI volumes, (e) preprocessed fMRI volumes, (f) cortical surface extracted from structural MRI with projected fMRI signals, (g) a decoded retinotopic map, (h) a raw retinotopic map projected on a flat surface, and (i) a registered retinotopic map.

2.1 Raw Retinotopic Map

2.1.1 Surface extraction

The structural MRI is used to construct the cortical surface using Freesurfer (Fischl and et al. 1999). We denote the discrete cortical surface by S_s, consist of vertices $V_s = \{V_i | i = 1,2,\dots,n\} = \{V_1, V_2, \dots, V_n\}$ and triangular faces F_s, i.e. $S_s = (F_s, V_s)$.

2.1.2 fMRI preprocessing

The goal of fMRI preprocessing is to detect the time series of brain activations of the voxels on the visual cortical surface that are associated with the visual stimuli. Typically, the raw fMRI data from each imaging session are co-registered across time to reduce the influence of head movements and other motion artifacts (**Fig.** 1e). Then the co-registered fMRI data are projected onto the cortical surface (**Fig.** 1f). During the projection, spatial smoothing may be applied along the cortical surface to improve the quality of the fMRI signals (Glasser et al. 2013). Finally, depending on the required resolution, resampling might be applied. After preprocessing, each vertex $V_i \in V_s$ on the surface $S_s = (F_s, V_s)$ is associated with a fMRI time series $y_i(t)$.

2.1.3 pRF decoder

For each vertex $V_i \in V_s$ on the cortical surface, the population receptive field analysis (pRF) (Dumoulin and Wandell 2008; Kay et al. 2013) is used to determine its receptive field, including its center location $\boldsymbol{v}$ and size σ in the unit of visual field.

Assuming that the population response model is $r(\boldsymbol{v}'; \boldsymbol{v}, \sigma)$ and the hemodynamic function is $h(t)$, the predicted blood-oxygen-level-dependent (BOLD) signal of the vertex can be written by:

$$\hat{y}(\boldsymbol{v}, \sigma) = \beta \left(\int r(\boldsymbol{v}'; \boldsymbol{v}, \sigma) s(t, \boldsymbol{v}') d\boldsymbol{v}' \right)^n * h(t), \quad (1)$$

where β is the activation level, which is invariant over time, n is exponent power. The perception center $\boldsymbol{v}$ and population receptive field size σ can be estimated by minimizing the squared difference between the measured and predicted BOLD signals:

$$(\boldsymbol{v}, \sigma, n) = \arg\min_{(\boldsymbol{v},\sigma)} |\hat{y}(\boldsymbol{v}, \sigma) - y(P)|^2, \quad (2)$$

where $y(P)$ is the BOLD signal at voxel P. The goodness of fit is evaluated by,

$$p_c = \frac{\sum_{i=1}^{n}(x_i - \bar{x})(y_i - \bar{y})}{\sqrt{\sum_{i=1}^{n}(x_i - \bar{x})^2}\sqrt{\sum_{i=1}^{n}(y_i - \bar{y})^2}} \quad (3)$$

where x is the predicted signal and y is the measured signal.

Iterations of this procedure across all the vertices on the visual cortical surface generate a collection of the pairing of V and $(\boldsymbol{v}, \sigma, R^2)$ and therefore the raw *retinotopic map*. We call it the *raw retinotopic map* to distinguish it from post-registration results. In addition, we use $S = (F_s, V_s, \boldsymbol{v}_s, \sigma_s, R_s^2)$ to denote the collection of cortical surface as well as the raw retinotopic map for subject s.

2.2 Registration

2.2.1 Mathematical model

Given a proper template T, which consists of a discrete triangular mesh together with predefined pRF parameters, including visual coordinates $\boldsymbol{v}_T$, receptive field size σ_T, and variance explained R_T^2 on each vertex, $T = (F_T, V_T, v_T, \sigma_T, R_T^2)$, registration is defined as a function $f' : \mathbb{R}^3 \to \mathbb{R}^3$ that minimizes the difference between a subject's raw retinotopic map and the template:

$$f' = \arg\min_{f'} E_R(f|S, T), \quad (4)$$

where $E_R(f'|S, T)$ is the registration energy for registration function f' for a given subject's raw retinotopic map S.

What is a proper registration function E_R? It is clear that the main term should be related to visual coordinate difference, $\sum_i |v_s(f_i) - v_t(i)|^2$, where $v_s(f_i)$ is the visual coordinate of the subject's registered retinotopic map at vertex *i,* and $v_t(i)$ is the template's visual coordinate at vertex *i*. In addition, the registration between cortical surface must be *diffeomorphic*.

To formulate the diffeomorphic condition, we simplify the registration problem by projecting the 3D retinotopic map diffeomorphically to a 2D parametric domain (Ta et al. 2014), and consider diffeomorphic registration in the 2D domain. As shown in **Fig.** 2, we first define a point which roughly corresponds to the fovea as the center. Second, we cut a geodesic disk (Martínez et al. 2005) (i.e. the distance along the surface from any point to the center is within a value) on the cortical surface. Then we map the geodesic disk to the 2D parametric domain by discrete conformal mapping $c: P \mapsto u$, where $u = \left(u^{(1)}, u^{(2)}\right) \in \mathbb{R}^2$ and $P \in \mathrm{V_s}$. The same operation is performed on the template retinotopic map (**Fig.** 2c gray color region) to project it to the parametric space $c': P' \mapsto u'$, $u = \left(u^{(1)}, u^{(2)}\right) \in \mathbb{R}^2$ and $P' \in \mathrm{V}_T$. If we can find a registration function $f: u \mapsto u'$ between the subject's and the templates' retinotopic maps in the 2D parametric space, we can write the registration for the two retinotopic maps as $f' = c'^{-1} \circ f \circ c$. Since both c and c' are given, the remaining problem is to find the 2D registration f.

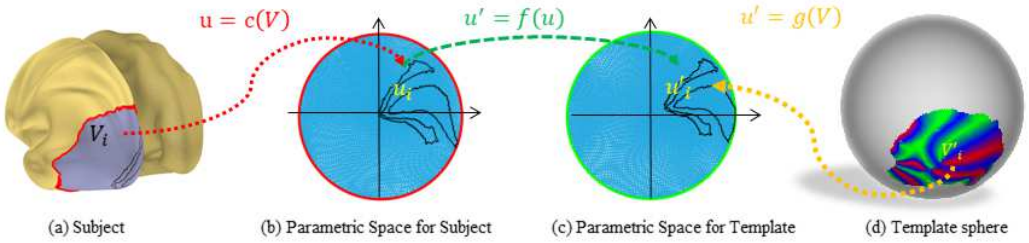

Figure 2. Illustration of several spaces and registration in the parametric space (the template sphere is rotated for illustration purpose.)

The 2D diffeomorphic registration f can be treated as a quasiconformal map by considering the 2D points as complex numbers, i.e., $f: \mathbb{C} \to \mathbb{C}$, and the diffeomorphic condition can be quantified by the *Beltrami coefficient* (Ahlfors and Earle 1966) for $f = f^{(1)} + if^{(2)}$. Specifically, the Beltrami coefficient is given by,

$$\mu_f = \left(\frac{\partial f}{\partial u^{(1)}} + i\frac{\partial f}{\partial u^{(2)}}\right) / \left(\frac{\partial f}{\partial u^{(1)}} - i\frac{\partial f}{\partial u^{(2)}}\right), i = \sqrt{-1}. \quad (5)$$

According to the Quasiconformal Theorem (Ahlfors and Earle 1966), *if* $\|\mu_f\|_\infty < 1$, *then* f *is diffeomorphic*. Moreover, the Beltrami coefficient uniquely encodes the quasiconformal mapping up to normalization (Ahlfors and Earle 1966), which provides a strategy to manipulate all diffeomorphic maps via a set of complex numbers.

With the diffeomorphic condition, we formulate the retinotopic registration problem by,

$$f = \arg\min_f \int w|v_s(f) - v_T|^2 + \lambda_s|\nabla f|^2 \, \mathrm{du}, s.t., \|\mu_f\|_\infty < 1, \quad (6)$$

where $w: \mathbb{R}^2 \to \mathbb{R}$ is a weight function and λ_s is a positive constant to encourage smoothness in the registration. Intuitively, **Eq.** 6 is used to find the registration f that (1) minimizes weighted visual coordinate differences (in terms of $w|v_s(f) - v_T|^2$); (2) is smooth (in terms of $\lambda_f|\nabla f|^2$), and (3) diffeomorphic (constrained by $\|\mu_f\|_\infty < 1$). Solving **Eq.** 6 generates a diffeomorphic registration, which enables preservation of the topological condition of the retinotopic map (Tu et al. 2020b). It is worth noting that, for each visual area, the topological condition can also be quantified by the Beltrami coefficient associated with the mapping from cortical surface to the visual space.

2.2.2. Numerical methods

Although we have defined the explicit registration energy, it is still computationally heavy to solve f directly. To have an efficient solution, we iteratively refine the alignment, ensure the diffeomorphic condition, and smooth the registration.

Improving alignment by the simple demon algorithm

We update the visual coordinate alignment by the simple demon algorithm (Thirion 1998), which moves each vertex in the source domain to match the target (template) visual coordinates. In the original algorithm, one choice is to move the subject's vertex location in the parametric domain by a displacement:

$$d = \frac{(I_s - I_m)\nabla I_m}{\nabla I_m + (I_s - I_m)^2}, \tag{7}$$

where I_s and I_m are the visual coordinates of the target (not moving) and source (moving). In our setting, we consider each component of the visual coordinate as the intensity and migrate them by the sum of the displacement. We denote $\bar{f} = u_s + \beta d$ as the result of simple demon registration, where β is the step size of the move. u_s is the parametric coordinate of the last iteration.

Diffeomorphic projection

$\bar{f}$ reduces visual coordinate difference but cannot ensure the diffeomorphic condition. One can make a diffeomorphic map by the following procedure: (1) compute the map's Beltrami coefficient μ, (2) adjust the Beltrami coefficient, such that that the new Beltrami coefficient μ' satisfies $\|\mu'\|_\infty < 1$, and (3) generate a new map from the new Beltrami coefficient. We now introduce the procedure in the discrete setting.

(1) Computing Beltrami Coefficient

Suppose we are given an analytical f, we can compute the Beltrami coefficient μ_f according to **Eq.** 5. However, in the discrete case, usually the function value is only given on each vertex, i.e., we only know the mapping between the source and target vertices (**Fig.** 3a): $v_i = f(u_i)$, $v_j = f(u_j)$, and $v_k = f(u_k)$. To approximate the derivatives, f is linearly interpreted on each triangle, i.e., for u within a triangle $\Delta u_i u_j u_k$, $f(u) = B_i v_i + B_j v_j + B_k v_k$. The coefficients B_i, B_j, B_k are called the barycentric coefficients. Intuitively, B_i (likewise for B_j and B_k) is the area portion of triangle $\Delta u u_j u_k$ to $\Delta u_i u_j u_k$, i.e. $B_i = \text{Area}(\Delta u u_j u_k)/\text{Area}(\Delta u_i u_j u_k)$. Now we can compute the Beltrami coefficient μ_f for each triangle according to **Eq.** 5. It is clear μ_f is a face-wise complex-valued constant, since f is linearly related to u and μ_f takes the first order partial derivative.

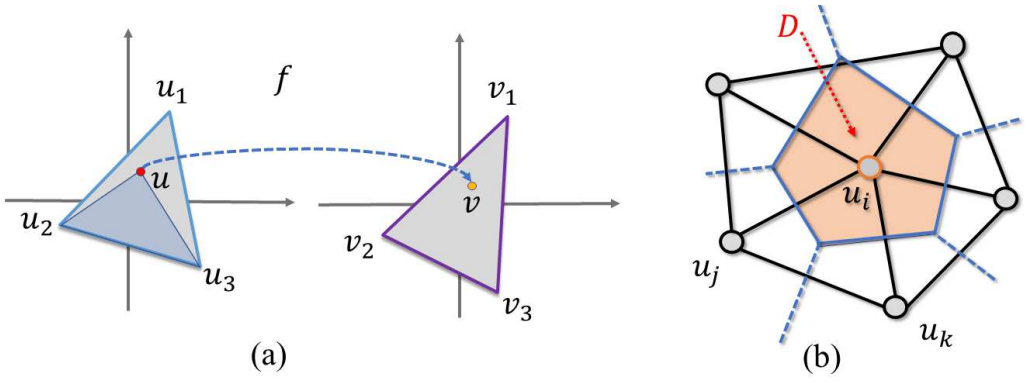

Figure 3. Illustration of a mapping function and the derivative computation. (a) an illustration of the mapping function in the discrete domain, and (b) divergence approximation for a vertex.

(2) Beltrami Projection

Once we compute the Beltrami coefficient μ, we apply following manipulation,

$$\mu' = \begin{cases} \mu/(|\mu| + \epsilon), & if\ |\mu| > 1 \\ \mu, & otherwise. \end{cases} \tag{8}$$

Since $\epsilon > 0$, $|\mu'|$ will be less than 1. Namely, we slightly adjust the Beltrami coefficient so that it corresponds to a diffeomorphic map.

(3) Recovering from the New Beltrami Coefficients

We now introduce the numerical method to recover function $\hat{f} = \hat{f}^{(1)} + i\hat{f}^{(2)}$ on the given Beltrami coefficient $\mu' = \rho + i\tau$. It was first introduced in (Lui et al. 2013) and called *Linear Beltrami Solver (LBS)*. According to the definition, i.e., **Eq.** 5, we have,

$$\left(\frac{\partial \hat{f}}{\partial u^{(1)}} + i\frac{\partial \hat{f}}{\partial u^{(2)}}\right) / \left(\frac{\partial \hat{f}}{\partial u^{(1)}} - i\frac{\partial \hat{f}}{\partial u^{(2)}}\right) = \rho + i\tau. \tag{9}$$

After re-organizing **Eq.** 9, it is equivalent to,

$$\begin{cases} -\frac{\partial \hat{f}^{(1)}}{\partial u^{(2)}} = \alpha_1 \frac{\partial \hat{f}^{(2)}}{\partial u^{(1)}} + \alpha_2 \frac{\partial \hat{f}^{(2)}}{\partial u^{(2)}} & \text{(10a)} \\ \frac{\partial \hat{f}^{(1)}}{\partial u^{(1)}} = \alpha_1 \frac{\partial \hat{f}^{(2)}}{\partial u^{(1)}} + \alpha_2 \frac{\partial \hat{f}^{(2)}}{\partial u^{(2)}} & \text{(10b)} \end{cases},$$

where $\alpha_1 = k(\tau^2 + (\rho - 1)^2)$, $\alpha_2 = -2k\tau$ and $\alpha_3 = k(1 + 2\rho + \rho^2 + \tau^2)$, $k = 1/(1 - \rho^2 - \tau^2)$. Now, apply $\partial/\partial u^{(1)}$ on **Eq.** 10a, apply $\partial/\partial u^{(2)}$ on **Eq.** 10b and sum them up, one can write,

$$\nabla \cdot A\nabla \hat{f}^{(1)} = 0, \tag{11}$$

where $A = \begin{pmatrix} \alpha_1 & \alpha_2 \\ \alpha_2 & \alpha_3 \end{pmatrix}$, $\nabla \hat{f}^{(1)} = (\partial \hat{f}^{(1)}/\partial u^{(1)} + \partial \hat{f}^{(1)}/\partial u^{(2)})$, and $\boldsymbol{\nabla} \cdot \boldsymbol{G}$ ($\boldsymbol{G} = A\nabla \hat{f}^{(1)}$ is called the *skewed gradient*) is defined as $\boldsymbol{\nabla} \cdot \boldsymbol{G} = \partial G^{(1)}/\partial \mathrm{u}^{(1)} + \partial G^{(2)}/\partial \mathrm{u}^{(2)}$. By solving the partial differential equation **Eq.** 11 with Dirichlet boundary condition, we can solve $\hat{f}^{(1)}$. Similarly, if we eliminate $\hat{f}^{(1)}$, we can write $\nabla \cdot A\nabla \hat{f}^{(2)} = 0$. After converting to the complex form $\hat{f} = \hat{f}^{(1)} + i\hat{f}^{(2)}$, these two partial differential equations can be summarized by $\nabla \cdot A\nabla \hat{f} = 0$.

In the discrete case, since the function is interpreted on each triangle, the gradient $\nabla \hat{f}^{(1)}$ can be written out on each triangle. Numerically, it is not precise to directly compute the divergence $\boldsymbol{\nabla} \cdot \boldsymbol{G}$ on discrete gradient. Instead, we use Stock's theorem (Gauss and Gauss 1877) to approximate the divergence of a triangle mesh vertex. As shown in **Fig.** 3b, the divergence is the average out-flux of skewed gradient $\boldsymbol{G}$ on its dual polygon D. Let $N(u_i)$ be the triangle set that each triangle u_i in $N(u_i)$ attaches to. The vertex-dual, D, is a polygon constructed from the circumcenters of the attached triangles $N(u_i)$. Since the skewed gradient $\boldsymbol{G}$ is constant on each triangle, the divergence can be written as,

$$\boldsymbol{\nabla} \cdot \boldsymbol{G}(u_i) = \frac{1}{|D|}\int_{\partial D} \boldsymbol{G} \cdot d\boldsymbol{l} = \frac{1}{|D|}\int_{\partial \mathrm{D}} \boldsymbol{G} \cdot d\boldsymbol{l} = \frac{1}{|D|}\sum_{T_j \in N(u_i)} \boldsymbol{G}_{T_j} \cdot (u_k - u_j), \tag{12}$$

where T_j is the j-th triangle in $N(u_i)$. According to **Eq.** 12, we have a linear equation with respect to f_i and its neighbors.

Eventually, we can write $\nabla \cdot A\nabla \hat{f} = 0$ in a matrix form: $\boldsymbol{L}\hat{f} = 0$, where $\hat{f} = [\hat{f}_1, \hat{f}_2, \dots, \hat{f}_{|V|}]$ and matrix $\boldsymbol{L}$ is defined as,

$$L_{i,j} = \begin{cases} \sum_{[\boldsymbol{u_i}, \boldsymbol{u_j}, \boldsymbol{u_k}] \in N(\boldsymbol{i})} \frac{(A\boldsymbol{s}_j) \cdot \boldsymbol{s}_i}{|[\boldsymbol{u}_i, \boldsymbol{u}_j, \boldsymbol{u}_k]|}, & \text{if } i \neq j \\ -\sum_{\boldsymbol{k} \neq \boldsymbol{i}} L_{i,k}, & \text{if } i = j \\ 0, & \text{otherwise.} \end{cases} \tag{13}$$

where $\boldsymbol{s}_i = \boldsymbol{n} \times (\boldsymbol{u}_j - \boldsymbol{u}_k)$, $\boldsymbol{s}_j = \boldsymbol{n} \times (\boldsymbol{u}_k - \boldsymbol{u}_i)$ and $\boldsymbol{n}$ is the face normal vector. The matrix form $\boldsymbol{L}\hat{f} = 0$ contains $|V|$ number of complex-valued equations. For the i-th equation, $L_{i,j}$ is the coefficient of

variables f_j, namely, $L_{i,1}\hat{f}_1 + L_{i,2}\hat{f}_2 + \cdots + L_{i,|V|}\hat{f}_{|V|} = 0$. Let $\boldsymbol{I}$ and $\boldsymbol{B}$ be the interior and boundary/landmark vertex indices, respectively. The discrete map $\hat{f}$ can be obtained by solving the linear equations $L_{\mathbf{I},\mathbf{I}}\hat{f}_{\mathbf{I}} = -L_{\mathbf{I},\mathbf{B}}\hat{f}_{\boldsymbol{B}}$, where $\hat{f}_{\boldsymbol{B}}$ is a sub-vector of $\hat{f}$ composed of $\hat{f}_j$ for $j \in \mathbf{B}$. The matrix $L_{\mathbf{I},\mathbf{B}}$ is a sub-matrix of L composed of $L_{i,j}$, for $i \in \mathbf{I}$ and $j \in \mathbf{B}$. The matrix $\hat{f}_{\boldsymbol{I}}$ and $L_{I,I}$ are similarly defined.

Smoothing

To make the registration smooth, we use Laplacian smoothing to find smoothed $\tilde{f}$ after diffeomorphic projection, such that,

$$\tilde{f} = \arg\min_{\tilde{f}} \int \left|\nabla\tilde{f}\right|^2 + \lambda_s\left|\tilde{f} - \hat{f}\right|^2 du, \tag{14}$$

where λ_s is defined in **Eq.** 6. By letting partial derivatives of **Eq.** 14 to be zero, it induces Euler-Lagrange equations: $(-\nabla\cdot\nabla + 2\lambda_s)\tilde{f} = 2\lambda_s\hat{f}$, which can be written in a matrix form, $(L' + 2\lambda_s I)\tilde{f} = 2\sigma\hat{f}$. Notice that I is the identity matrix, and $L' = \boldsymbol{\nabla}\cdot\nabla$ is the special case when A is an identical matrix in **Eq.** 13. So, we can also write L' in a matrix form and solve $\tilde{f}$ efficiently.

The registration results are influenced by the smooth parameter λ_s. We use a *generalized cross-validation* (GCV) procedure to estimate the proper parameter to avoid both over-smoothing and under-smoothing. The GCV procedure was initially introduced by (Craven and Wahba 1978) in smoothing splines. Assuming that for each subject, there are $n = |V|$ raw visual coordinate measurements, denoted by $f_1, f_2, \ldots, f_n$. We uniformly split the data into 5 distinct folds, $F_1 = \{f_i | i \in K_1\}, F_2 = \{f_i | i \in K_2\}, \ldots, F_5 = \{f_i | i \in K_5\}$, where K_j is the index set of the j-th fold. Leaving out the k −th fold, F_k, we can use the rest four folds to compute the smoothed results on a specific λ_s, denoted by $\tilde{f}^k_{\lambda_s}$. Then, we can estimate the error between the smoothed and raw visual coordinates within fold k. Eventually, we can find the optimal parameter λ_s that minimizes the overall difference (sum over $k = 1, 2, \ldots, 5$). Mathematically,

$$\lambda_s = \arg\min_{\lambda_s} \sum_{k=\{1,\ldots,5\}} \sum_{i\in F_k} D_i\left(f_i - \tilde{f}^k_{\lambda_s,i}\right)^2, \tag{15}$$

where D_i is the area-weight for vertex i (**Fig.** 3b). In practice, we used the grid resampling (Garcia 2010) data in the disk (resample with 200x200 grid for the parametric unit disk) to approximate the estimation of λ_s.

2.2.3. Algorithm

We summarize the *Diffeomorphic Registration for Retinotopic Maps (DRRM)* algorithm in **Alg.** 1.

Algorithm 1. *Diffeomorphic Registration for Retinotopic Maps*

Data: Subject's raw retinotopic map $S = (F_S, V_S, v_s, \sigma_s, R_S^2)$, template retinotopic map $T = (F_T, V_T, v_T, \sigma_T, R_T^2)$, and threshold ϵ.

Result: Registration function f from the subject raw retinotopic map to the template retinotopic map.

1. Compute conformal parametrization for subject $u_s = c_s(F_S, V_S)$, and template $u_T = c_T(F_T, V_T)$;
2. Take identity mapping as initial, $f(u_s) \leftarrow u_s$;
3. repeat
   a) Update registration function $\bar{f}$ regardless of diffeomorphism, according to **Eq.** 7.
   b) Compute Beltrami coefficient μ for $\bar{f}$, according to **Eq.** 5.
   c) Project Beltrami coefficient to get μ', according to **Eq.** 8.
   d) Compute diffeomorphic mapping $\hat{f}$ by LBS on the projected coefficient μ';
   e) Apply Laplacian smoothing to get $\tilde{f}$ from $\hat{f}$, according to **Eq.** 14.
   f) Compute $\delta f = \max\left|\tilde{f} - f\right|$, and update $f \leftarrow \tilde{f}$
4. until $\delta f < \epsilon$ and $\|\mu\|_\infty < 1$
5. return f.

2.3 Data and Atlas

We applied DRRM to one synthetic and two real retinotopy datasets. The synthetic data is mainly used to compare the registration performance of DRRM with other state-of-the-art methods. Two real retinotopic map datasets, Human connectome project (HCP) (Kay et al. 2018) and Studyforrest (Sengupta et al. 2016), are used to demonstrate the application of DRRM to human retinotopic maps.

2.3.1 Synthetic data

We generated a synthetic dataset that included subject and template retinotopic maps using the double-sech model proposed by Schira et al. (2010):

$$u^{(1)} + iu^{(2)} = k \cdot \ln\left(v^{(1)} \cdot \exp\left(iv^{(2)} \cdot f_a\right) + a\right), \tag{16}$$

where $f_a = \operatorname{sech}\left(v^{(2)}\right)^{0.18*\operatorname{sech}\left(0.76\log\left(v^{(1)}/a\right)\right)}$, $a = 10$, and $b = 90$. The model is applicable to V1-V3 simultaneously by setting a shear value s for each area and concatenating them along with $v^{(2)}$. Namely, $v^{(2)}$ in **Eq.** 16 is concatenated by $v^{(2)} = \left\{s_1 v_i^{(2)} | v_i \in V_1\right\} \cup \left\{s_2\left(v_i^{(2)} \pm s_1\pi/2\right) | v_i \in V_2\right\} \cup \left\{s_3\left(v_i^{(2)} \pm s_1\pi/2 \pm s_2 s_1\pi\right) | v_i \in V_3\right\}$. We can generate different retinotopic maps by manipulating the parameters.

We started with visual coordinates on a grid and used the model with $s_1 = 0.4, s_2 = 0.25$, and $s_3 = 0.2$ for V1, V2, and V3, respectively to generate the template, and $s_1 = 0.5, s_2 = 0.3$, and $s_3 = 0.15$ to generate the subject's retinotopic maps in V1/V2/V3. In the ideal case, the retinotopic maps of the subject and template can be fully aligned after registration.

Then we enclosed both subject and template into a unit circle. We then generated the triangular mesh on the disk. This step is to ensure the data is of same format as real dataset where we map to disks during the registration.

2.3.2 HCP retinotopy data

The Human connectome project (HCP) (Kay et al. 2018) provides a large publicly available retinotopy dataset collected on 7T MRI scanners. The data collection, conducted on 181 healthy young adults (22-35 years; 109 females, and 72 males) with normal or corrected-to-normal visual acuity, involved carefully designed retinotopy stimuli and resulted in a substantial amount of fMRI data (30 min, 1,800 time-points) acquired at very high spatial and temporal resolutions (1.6 mm isotropic voxels, 1-second temporal sampling). The dataset provides an exciting opportunity to compare the registration methods. It was pre-processed by the HCP group to 32k mesh (Glasser et al. 2013). Here, we computed the pRF parameters using analyzePRF (Version 1.1) (Kay et al. 2013), with the following setting: (1) cubically detrend the fMRI signal; (2) stimulation image size 200x200; (3) compressive model with big receptive field size seed.

2.3.3 Studyforrest retinotopy data

The Studyforrest dataset (Sengupta et al. 2016) consists of 15 observers' fMRI data from the travelling wave experiment for retinotopic map on a 3T MRI system. The data are processed in the following steps. First, the T1 weighted structural images were used to reconstruct the cortical surface by Freesurfer (version 5.3.0) (Fischl and et al. 1999). Then we resampled the surface to 59k vertices. We then preprocessed the fMRI data: (1) we used SPM (Friston et al. 1996) (Version 12) to correct slice timing; (2) we used SPM to align all the fMRI volumes to the first volume for each run of the retinotopic experiment, including the expanding ring, contracting ring, clock-wise rotated wedge, and counter clock-wise rotated wedge; (3) Then we projected the fMRI signal to the mid-surface (between pial and white) generated from Freesurfer. Once we have the fMRI signal on the surface, we used Kay's analyzePRF

(Version 1.1) to decode the fMRI signal with following settings: (1) linearly detrend the signal; (2) stimulation image size 640x640; (3) with traveling wave results (provided by https://github.com/psychoinformatics-de/studyforrest-data-retinotopy) as perception center seed for each vertex, and (4) compressive pRF model with big receptive field size seed. The data and code for reproducing the results are available on the OSF website https://osf.io/s25pe/.

2.3.4 Retinotopic template

We started with Benson and Winawer's retinotopic model (Benson and Winawer 2018) and the group-average retinotopic map from the HCP group $T_0 = \left(F_{T_0}, V_{T_0}, v_{T_0}, \sigma_{T_0}, R^2_{T_0}\right)$. We first transferred the BW retinotopic model from the "*fsaverage*" space to the "*fsLR*" space, and then followed the technique introduced in **Sec**. 2.2 to align it to T_0. The morphed template, denoted by $T = (F_T, V_T, v_T, \sigma_T, R^2_T)$, was used as the template in DRRM for our registration.

2.4 Performance Evaluations

We compared DRRM with several popular retinotopic and image registration methods, including Thin Plate Spline TPS (Sprengel et al), Bayesian (Benson and Winawer 2018), and D-Demos (Vercauteren et al. 2009).

TPS is a widely used non-rigid transformation method, which treats registration as two displacement functions approximated by two thin plate surfaces. To find these surfaces, landmark points are defined on both the source and target surfaces. TPS interpolates the thin plate surfaces based on the landmarks. Therefore, the precision of the registration results is dominated by the quality of the landmarks but not the other visual coordinates.

Benson and Winawer's Bayesian registration framework, which we call the "Bayesian method" for short, adopts a mass-spring-damp phiolophy to align subjects' retinotopic maps to the template (Benson and Winawer 2018). It is a very intuitive method that treats edges as springs and nodes as mass balls. To encourage alignment of high quality points, well-potentials can be set to attract the mass balls to specific areas. Here, we set landmarks with infinite well. Because they are given by the experimenter, the landmarks define high quality points in retinotopic maps.

D-Demos is a popular diffeomorphic image registration method that projects the results from the simple-demon algorithm in each iteration to be diffeomorphic. One limitation of the simple demon is that it does not provide diffeomorphic registration. In D-Demos, diffeomorphic registration is achieved by projecting the displacements from the simple-demon algorithm to the space of diffeomorphic transformations in each iteration (e.g., by Jacobian).

Both TPS and D-Demos were designed for image registration and have not been used in retinotopic registration. We applied them to images with intensity determined by the eccentricity visual coordinates of the retinotopic maps first and then images with intensity determined by the polar angle visual coordinates second and reiterated the process several times.

For the synthetic dataset, because we have the ground-truth displacement, we mainly compared the performance of these registration methods using the ***Registration Displacement Error***. In addition, to evaluate whether the registration function is diffeomorphic, we calculated the number of ***flipped triangles***, $\boldsymbol{F_{flip}}$, in the registration function. If $F_{flip} = 0$, the registration function is diffeomorphic.

For the real retinotopic datasets, because there is no ground truth, we evaluate the performance of registration by two types of metrics. The first type is about registration performance, including the magnitude of ***visual coordinate change to ensure topological*** ($d|v|$) and the number of flipped triangles, F_{flip}. More specifically, $d|v|$ is the average of point-wise visual coordinate change which is calculated by the Euclidian distance between raw visual coordinate and the template-interpretated visual coordinate

after registration. The second type metrices is related to the goodness of fit to the BOLD time series, including the Root Mean Square Error (***RMSE***), **Akaike information criterion** (***AIC***), and ***Pearson correlation*** (p_c) defined in **Eq.** 3. Specifically, after registration, the parametric positions of the subject's retinotopic maps were adjusted. We interpreted the visual coordinates of the vertices on the subject's retinotopic maps from the template. If the registration is good, Reg. Error is small, which means the visual coordinate differences between the subject's registered retinotopic maps and the template are small. If the RMSE is small, the registered retinotopic maps fit the BOLD signals well. Similarly, if the AIC is smaller, the registered retinotopic maps explain the data better with the same number of parameters; if the Pearson correlation is greater, the registered retinotopic maps explain the BOLD signal better. Since the template we adopted is topological, the registered retinotopic maps is topological when $F_{flip} = 0$.

3. RESULTS

3.1 Performance on Synthetic Data

We first calculated the ground-truth displacement based on the parameters of the generative model (**Eq.** 16) for the subject and template and generated noisy data for registration (**Fig.** 4).

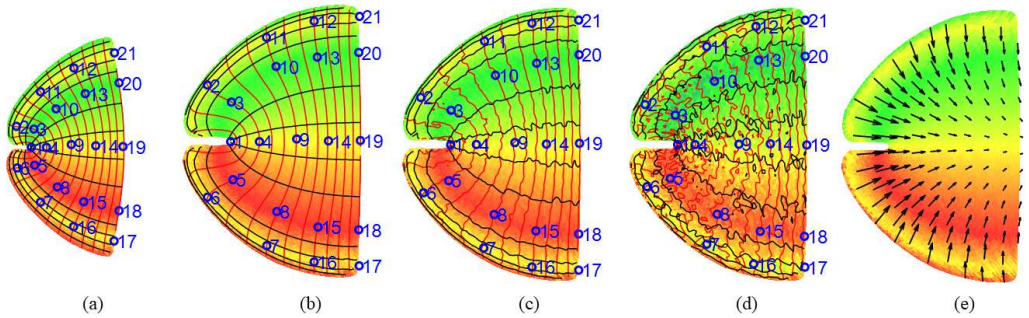

Figure 4. Template and Subject Retinotopic Maps (synthetic data): (a) The predefined template; (b) noiseless retinotopic map of a subject; (c) retinotopic map of a subject with weak noise (PSNR = 20); (d) retinotopic map of a subject with strong noise (PSNR = 10); (e) ground truth displacement. Red curves are eccentricity contours, black curves are polar angle contours, and some landmarks/anchors are marked in (a)-(d).

The performance metrics for the four methods are listed in **Tab.** 1. To evaluate the influence of noise on registration results, we reported each value with two levels of noise (PSNR = 20 and 10) and separated them by "/".

Method	**Registration Displacement Error**		F_{flip}
	Mean	Max	
TPS*	0.59/0.59	1.19/1.19	0/0
Bayesian*	0.86/0.86	1.66/1.66	1/0
D-Demos	1.77/1.77	2.54/2.54	0/0
DRRM*	**0.44/0.44**	**0.97/0.96**	**0/0**

Table 1. Comparing registration performance relative to the ground truth. Each cell has two values, for the low and high fMRI noise conditions, respectively. Landmarks (the circled positions in **Fig.** 4) were used if the method accepts them (marked with "*" symbol); We conducted the same experiment in both noise settings. The results are separated by "/".

We found that (1) DRRM achieved the smallest registration displacement error and ensured the diffeomorphism ($F_{flip} = 0$) in both conditions; (2) TPS, which moves the landmarks to match targets and interpolates the rest of the maps by smooth spline, was the fastest method. However, its precision was dominated by the quality of the landmarks but not the visual coordinates for the rest of the region; (3) The D-Demos method can ensure diffeomorphic results for image registration. However, distortions may be introduced by treating the visual coordinates as two separate images and registering them iteratively; (4) The Bayesian method was proposed specifically for retinotopic registration. However, it had many tuning parameters, and it is difficult to achieve diffeomorphic registration with small errors.

3.2 Human Retinotopic Template

The group-average retinotopic map from the HCP group was cut and conformally mapped to the 2D parametric disk (**Figs.** 5ab), i.e., $u = c(V_T)$. It formed a closed region in the fsLR sphere. Let the mapping from cortical surface to the fsLR sphere be $V_{sphere} = g(V_T)$, then the mapping from fsLR to the disk is given by $h = c \circ g^{-1}$, which maps from the fsLR sphere to the disk. We then fixed h and h^{-1} so that subjects' retinotopic maps can be mapped to the same disk with Freesurfer's spherical registration.

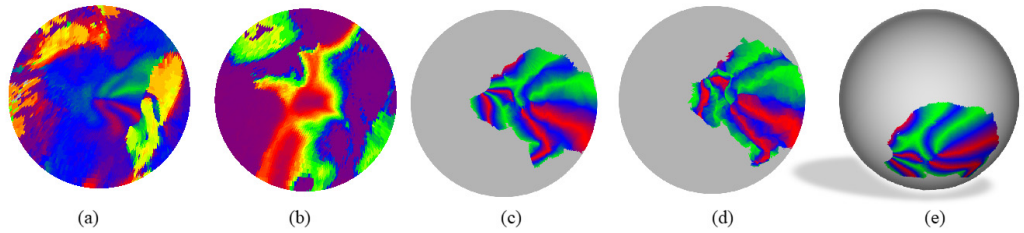

Figure 5. The Human Retinotopic Template (left hemisphere). (a) decoded polar angles of the group-average HCP retinotopic map in the disk domain; (b) decoded eccentricities of the group-average HCP retinotopic map in the disk domain, (c) BW's retinotopic model in the 2D domain, (d) the final template, (e) the template on the fsLR sphere.

We then transferred BW's retinotopic model (defined on the fsaverage sphere) to the fsLR space (by a rotation) and mapped it to the 2D disk by h (**Fig.** 5c). After registering the flattened BW retinotopic model (**Fig.** 5c) to the average HCP retinotopic map (**Figs.** 5ab), we obtained a new retinotopic model (**Fig.** 5d), which was our template and can be projected back to the "fsLR" sphere (**Fig.** 5e) by h^{-1}.

3.3 Registration of the retinotopic maps in HCP

We applied DRRM to register individual subject's V1/V2/V3 retinotopic maps in the HCP dataset to the template. The results for the first observer's left hemisphere are shown in **Fig.** 6. Specifically, the subject's raw pRF results (**Figs.** 6ab) were registered to the template (**Fig.** 5d) using DRRM. The registered results are shown in **Figs**. 6cd.

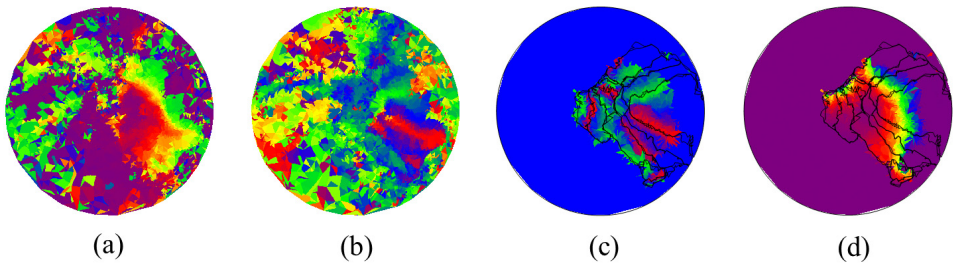

Figure 6. Before and after registration for the first observer: (a) the eccentricity of first subject, (b) polar angle of first subject, (c) registered polar angle, and (d) registered eccentricity. In (c)(d), data with eccentricity >8° are removed for clear comparation (since subjects' max eccentricity is 8°).

Method	$d\|v\|$	F_{flip}	RMSE	p_c	AIC
Raw	3.19844	**0**	1.15413	0.277	926.628
TPS*	3.83371	**0**	1.11658	0.297	905.461
Bayesian*	7.77147	23	1.14420	0.217	924.339
D-Demos	3.49798	**0**	1.10149	0.315	896.865
DRRM (proposed)	**2.57908**	**0**	**1.09772**	**0.328**	**885.839**

Table 2. Comparing registration performance by registration error, predicting RMSE, Pearson Correlation, and AIC metric in V1/V2/V3 for the first subject. Landmarks/anchors are given for method marked with "*" symbol.

Tab. 2 lists performance metrics of five registration methods. The "Raw" method did not touch the 2D positions of the subjects' retinotopic maps and directly used the template's visual coordinates. Since the HCP's retinotopic data has been pre-aligned by the MSMALL pipeline (Glasser et al. 2013), the "Raw" results are in fact from Multimodal Surface Matching (Robinson et al. 2018). DRRM achieved the minimum $d|v|$, and provided the best fit to the BOLD time series (AIC=885.8 vs AICs>896).

We also applied DRRM to the V1/V2/V3 retinotopic maps of the first five observers in the HCP dataset. The results are listed in **Tab**. 3. Registered retinotopic maps with DRRM fit the fMRI time series better than the "Raw" method in 9 out of 10 instances. The reduced RMSE from the DRRM fits means that the registered visual coordinates were closer to the original pRF solutions.

HCP Observers	$d\|v\|$	F_{flip}	RMSE		p_c		AIC	
			Raw	Reg.	Raw	Reg.	Raw	Reg.
Observer 1 (L)	3.198	0	1.21750	**1.19309**	0.212	**0.232**	958.730	**940.923**
Observer 1 (R)	1.806	0	1.18928	**1.14984**	0.255	**0.299**	943.992	**921.975**
Observer 2 (L)	3.769	0	1.25944	**1.19427**	0.125	**0.198**	984.375	**949.851**
Observer 2 (R)	2.586	0	1.23543	**1.22117**	0.165	**0.180**	969.625	**962.295**
Observer 3 (L)	2.764	0	1.27915	**1.27349**	0.144	**0.173**	993.547	**991.139**
Observer 3 (R)	2.796	0	1.20621	**1.19763**	0.209	**0.240**	958.584	**952.908**
Observer 4 (L)	3.213	0	1.23915	**1.13653**	0.179	**0.287**	972.463	**912.921**
Observer 4 (R)	3.167	0	**1.23483**	1.27859	**0.175**	0.130	**967.670**	993.482
Observer 5 (L)	2.598	0	1.20925	**1.13850**	0.252	**0.315**	959.236	**917.050**
Observer 5 (R)	2.698	0	1.14223	**1.13958**	0.286	**0.304**	912.874	**912.342**

Table 3. Performance of DRRM-registered retinotopic maps of the first five observers in the HCP retinotopy dataset relative to "Raw" retinotopic maps in V1-V3 (7T).

3.4 Improving 3T Retinotopic Maps

We also applied DRRM to the Studyforrest retinotopy dataset (Sengupta et al. 2016). Results for the first subject are shown in **Fig.** 7. The raw retinotopic eccentricity (**Fig.** 7a) and polar angle (**Fig.** 7b) results were drawn on the inflated surface for the first subject's left hemisphere. Then the results were transferred to the parametric disk (**Figs**. 7cd). After the registration, we updated visual coordinates for the subject (**Figs.** 7efgh).

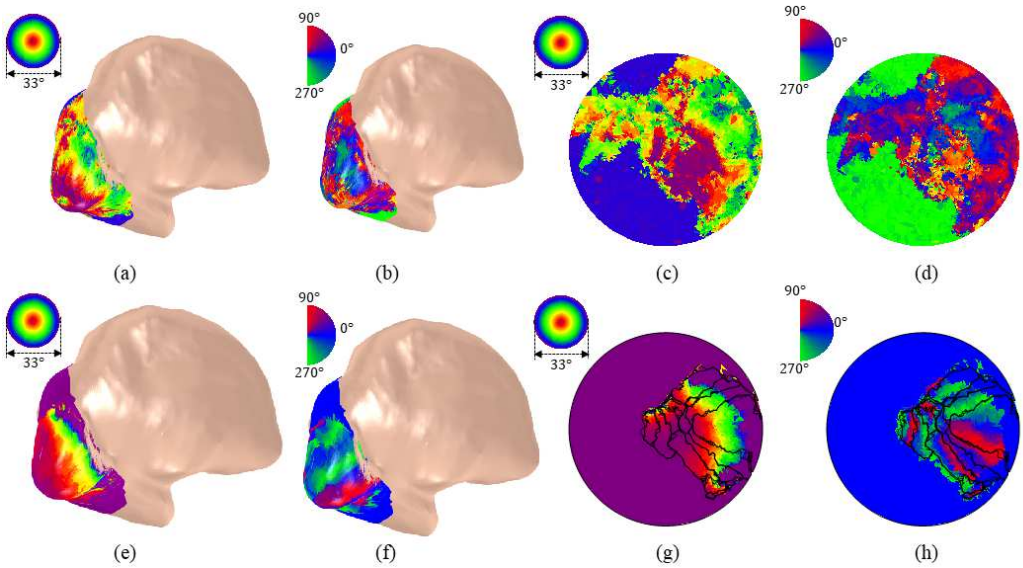

Figure 7. Retinotopic map on the left-hemisphere of the first observer in Studyforrest retinotopy dataset (Sengupta et al. 2016). (a) eccentricity map, (b) polar angle map, (c) eccentricity map on the disk, and (d) polar angle map on the disk. (e)-(h) shows the registered results correspondingly.

The performance metrics of DRRM-registered and the raw retinotopic maps of the first five observers are listed in **Tab**. 4. The raw retinotopic maps were inferred from Freesurfer's registration sphere. We found no flipping triangles, indicating that DRRM was diffeomorphic. Registered retinotopic maps with DRRM fit the fMRI time series better than the raw retinotopic maps in 7 out of 10 instances. The reduced RMSE from the DRRM fits means that the registered visual coordinates were closer to the original pRF solutions. The results suggest that the DRRM-registered retinotopic maps fit the fMRI time series better than structurally registered retinotopic maps.

Studyforrest Observers	$d\|v\|$	F_{flip}	RMSE		p_c		AIC	
			Raw	Reg.	Raw	Reg.	Raw	Reg.
Observer 1 (L)	12.296	**0**	1.3715	**1.3531**	0.041	**0.053**	209.235	**207.428**
Observer 1 (R)	12.226	**0**	1.1966	**1.1536**	0.127	**0.186**	191.380	**185.485**
Observer 2 (L)	12.169	**0**	1.3980	**1.3493**	0.016	0.013	211.553	**206.640**
Observer 2 (R)	12.432	**0**	1.2992	1.3388	0.098	0.041	201.517	204.709
Observer 3 (L)	12.828	**0**	1.3938	**1.3775**	-0.004	-0.005	211.007	**209.378**
Observer 3 (R)	11.953	**0**	1.3150	**1.3028**	-0.021	**-0.015**	202.969	**201.753**
Observer 4 (L)	12.550	**0**	1.3956	1.4172	-0.007	-0.022	211.184	213.208
Observer 4 (R)	11.604	**0**	1.3124	**1.3058**	0.049	**0.059**	203.362	**202.649**
Observer 5 (L)	10.892	**0**	1.3658	1.3743	0.047	0.002	208.607	209.172
Observer 5 (R)	11.184	**0**	1.3098	**1.2805**	0.024	**0.067**	202.630	**199.730**

Table 4. Performance of DRRM-registered retinotopic maps of the first five observers of Studyforrest retinotopy dataset (Sengupta et al. 2016) relative to structurally registered retinotopic maps V1-V3 (3T).

4. DISCUSSION

In this work, we proposed a novel *Diffeomorphic Registration for Retinotopic Maps (DRRM)* to simultaneously register retinotopic maps of multiple visual regions. We introduced the Beltrami coefficient to ensure diffeomorphism in registering the visual coordinates of individual subject's retinotopic maps to the template. We applied DRRM to synthetic, and real 7T and 3T retinotopic map

datasets. We found that DRRM can preserve the diffeomorphic condition with optimized smoothness. Because we reduced unnecessary constraints and quantified the diffeomorphic condition in a more fundamental way, our registration method had more flexibility to align the subjects' retinotopic maps to the template, compared with the spring-mass-damp system. Compared with D-Demons, the diffeomorphic space is favored in retinotopic maps: because retinotopic maps are approximately conformal (Schwartz 1977), the Beltrami coefficient is a good formulation after we conformally map the cortical surface to the 2D disk. In addition, DRRM was validated by the improved goodness of fit to the BOLD time series from both 7T and 3T retinotopy datasets. The goodness of fit metrics evaluates the performance of registration methods in terms of their ability to account for measurements. To our best knowledge, this is the first time that they are used to evaluate retinotopic map registration methods.

One major advantage of diffeomorphic registration is the preservation of the topological condition (Tu et al. 2020b): nearby neurons have receptive fields at nearby locations on the retina (Wandell et al. 2007). The raw pRF results cannot ensure such condition. Aligning a subject's retinotopic map to a topological template would make the post-registration retinotopic topological and make it possible to accurately quantify properties of the retinotopic maps, including cortical magnifications, angle distortions, boundary differences, etc. In addition, diffeomorphic registration can be used to automatically infer the boundaries of the visual areas, avoiding tedious and error-prone manual labeling. Moreover, because most visual boundaries are provided by structural registration with Freesurfer, some of the visual areas may be misplaced and eventually hidden after averaging. A diffeomorphic registration can emphasize retinotopic features and enable better identification of visual areas (Glasser and van Essen 2011).

There are numerous imperfections in retinotopic map data, arising from many sources, including partial volume effects of fMRI, eye movements during the experiment, and various sources of physiological and environmental noise. The question is: Does registration really improve the quality of retinotopic maps? This is a fundamentally challenging question. From the goodness of fit perspective, a method that accounts for more variance of the fMRI time series is better. However, over-fitting can be achieved with more complex models. Because it improved the goodness of fit without increasing the number of parameters compared to the pRF model and generated registered retinotopic maps that satisfy the topological condition (Wandell et al. 2007), we conclude that DRRM could improve the quality of retinotopic maps. With more accurate registration, our work may improve the interpretation of low-quality retinotopic maps and facilitate adoption of retinotopic maps in clinical settings.

Despite the promising results, there are two caveats in our work. First, the retinotopic template is based on the prior knowledge about the visual regions. To our knowledge, there are other retinotopic templates with different topologies (e.g., Wang et al. 2015). These templates have different visual area delineations in higher-level vision areas. In future, we need to adopt the same framework with different templates to identify the best template. Second, we have run Benson and Winawer's code with our data without tuning the hyper-parameters in the Bayesian registration method (Benson and Winawer 2018). Therefore, their results might be improved after more parameter tuning. Even so, the proposed DRRM method reduced some redundant constraints associated with edge shrinkage, angle shrinkage, and face shrinkage in the Bayesian registration framework.

5. CONCLUSIONS AND FUTURE WORK

We proposed a DRRM framework to simultaneously register retinotopic maps of multiple visual regions. We introduced Beltrami coefficient to monitor and maintain the topological condition, designed an

iterative algorithm to achieve both diffeomorphism and topological condition preservation, and conducted extensive experiments to compare DRRM with other retinotopic map registration methods with different testing datasets. Compared with the state-of-the-art methods, DRRM achieved better accuracy and provided better fits to BOLD fMRI time series. In future, we plan to further improve the retinotopic template based on our new registration results. Furthermore, with the refined registration results, we will develop a hierarchical Bayesian approach (Lu and Dosher 2013; Molloy et al. 2018) to integrate information at both individual and population levels and/or across multiple visual areas.

REFERENCES

Ahlfors L V, Earle CJ (1966) Lectures on Quasiconformal Mappings. Van Nostrand

Benson NC, Butt OH, Brainard DH, Aguirre GK (2014) Correction of Distortion in Flattened Representations of the Cortical Surface Allows Prediction of V1-V3 Functional Organization from Anatomy. PLoS Comput Biol 10:e1003538. https://doi.org/10.1371/journal.pcbi.1003538

Benson NC, Winawer J (2018) Bayesian analysis of retinotopic maps. Elife 7:. https://doi.org/10.7554/eLife.40224

Conner IP, Sharma S, Lemieux SK, Mendola JD (2004) Retinotopic organization in children measured with fMRI. J Vis 4:. https://doi.org/10.1167/4.6.10

Craven P, Wahba G (1978) Smoothing noisy data with spline functions - Estimating the correct degree of smoothing by the method of generalized cross-validation. Numer Math 31:377–403. https://doi.org/10.1007/BF01404567

Dumoulin SO, Wandell BA (2008) Population receptive field estimates in human visual cortex. Neuroimage 39:647–660. https://doi.org/10.1016/j.neuroimage.2007.09.034

Fischl B, et al. (1999) Cortical Surface-Based Analysis: II: Inflation, Flattening, and a Surface-Based Coordinate System: II: Inflation, Flattening, and a Surface-Based Coordinate System. Neuroimage 9:195–207

Friston KJ, Williams S, Howard R, et al (1996) Movement-related effects in fMRI time-series. Magn Reson Med 35:346–355. https://doi.org/10.1002/mrm.1910350312

Garcia D (2010) Robust smoothing of gridded data in one and higher dimensions with missing values. Comput Stat Data Anal 54:1167–1178. https://doi.org/10.1016/J.CSDA.2009.09.020

Gardiner FP, Lakic N (2000) Quasiconformal Teichmüller theory. American Mathematical Society

Gauss CF, Gauss CF (1877) Theoria attractionis corporum sphaeroidicorum ellipticorum homogeneorum, methodo nova tractata. In: Werke. Springer Berlin Heidelberg, Berlin, Heidelberg, pp 279–286

Glasser MF, Coalson TS, Robinson EC, et al (2016) A multi-modal parcellation of human cerebral cortex. Nature 536:171–178. https://doi.org/10.1038/nature18933

Glasser MF, Sotiropoulos SN, Wilson JA, et al (2013) The minimal preprocessing pipelines for the Human Connectome Project. Neuroimage 80:105–124. https://doi.org/10.1016/j.neuroimage.2013.04.127

Glasser MF, van Essen DC (2011) Mapping human cortical areas in vivo based on myelin content as revealed by T1- and T2-weighted MRI. J Neurosci 31:11597–11616. https://doi.org/10.1523/JNEUROSCI.2180-11.2011

Hubel DH, Wiesel TN (1962) Receptive fields and functional architecture of monkey striate cortex. J Physiol 160:106–54. https://doi.org/10.1113/jphysiol.1968.sp008455

Joshi AA, Shattuck DW, Thompson PM, Leahy RM (2007) Surface-constrained volumetric brain registration using harmonic mappings. IEEE Trans Med Imaging 26:1657–1668. https://doi.org/10.1109/TMI.2007.901432

Kay KN, Winawer J, Mezer A, Wandell BA (2013) Compressive spatial summation in human visual cortex. J Neurophysiol 110:481–494. https://doi.org/10.1152/jn.00105.2013

Kay N, Benson C, Jamison K, et al (2018) The HCP 7T Retinotopy Dataset. In: osf. https://osf.io/bw9ec/

Li X, Dumoulin SO, Mansouri B, Hess RF (2007) The fidelity of the cortical retinotopic map in human amblyopia. Eur J Neurosci 25:1265–1277. https://doi.org/10.1111/j.1460-9568.2007.05356.x

Lu Z, Dosher B (2013) Visual Psychophysics: From Laboratory to Theory, MIT Press.

Lui LM, Lam KC, Wong TW, Gu X (2013) Texture map and video compression using Beltrami representation. SIAM J Imaging Sci 6:1880–1902. https://doi.org/10.1137/120866129

Martínez D, Velho L, Carvalho PC (2005) Computing geodesics on triangular meshes. Comput Graph 29:667–675. https://doi.org/10.1016/j.cag.2005.08.003

Molloy MF, Bahg G, Li X, et al (2018) Hierarchical Bayesian Analyses for Modeling BOLD Time Series Data. Comput Brain Behav 1:184–213. https://doi.org/10.1007/s42113-018-0013-5

Qiu A, Bitouk D, Miller MI (2006a) Smooth functional and structural maps on the neocortex via orthonormal bases of the Laplace-Beltrami operator. IEEE Trans Med Imaging 25:1296–1306. https://doi.org/10.1109/TMI.2006.882143

Qiu A, Rosenau BJ, Greenberg AS, et al (2006b) Estimating linear cortical magnification in human primary visual cortex via dynamic programming. Neuroimage 31:125–138. https://doi.org/10.1016/j.neuroimage.2005.11.049

Robinson EC, Garcia K, Glasser MF, et al (2018) Multimodal surface matching with higher-order smoothness constraints. Neuroimage 167:453–465. https://doi.org/10.1016/j.neuroimage.2017.10.037

Robinson EC, Jbabdi S, Glasser MF, et al (2014) MSM: A new flexible framework for multimodal surface matching. Neuroimage 100:414–426. https://doi.org/10.1016/j.neuroimage.2014.05.069

Schira MM, Tyler CW, Spehar B, Breakspear M (2010) Modeling Magnification and Anisotropy in the Primate Foveal Confluence. PLoS Comput Biol 6:e1000651

Schwartz EL (1977) Spatial mapping in the primate sensory projection: Analytic structure and relevance to perception. Biol Cybern 25:181–194. https://doi.org/10.1007/BF01885636

Sengupta A, Kaule FR, Guntupalli JS, et al (2016) A studyforrest extension, retinotopic mapping and localization of higher visual areas. Sci Data 3:. https://doi.org/10.1038/sdata.2016.93

Shattuck DW, Leahy RM (2002) BrainSuite: an automated cortical surface identification tool. Med Image Anal 6:129–42

Swindale N V. (2000) How Many Maps are there in Visual Cortex? Cereb Cortex 10:633–643. https://doi.org/10.1093/cercor/10.7.633

Ta D, Shi J, Barton B, et al (2014) Characterizing human retinotopic mapping with conformal geometry: a preliminary study. In: Ourselin S, Styner MA (eds) Medical Imaging 2014: Image Processing. p 90342A

Thirion JP (1998) Image matching as a diffusion process: An analogy with Maxwell's demons. Med Image Anal 2:243–260. https://doi.org/10.1016/S1361-8415(98)80022-4

Tu Y, Ta D, Gu X, et al (2020a) Diffeomorphic Registration for Retinotopic Mapping Via Quasiconformal Mapping. In: Proceedings - International Symposium on Biomedical Imaging. IEEE Computer Society, pp 687–691

Tu Y, Ta D, Lu ZL, Wang Y (2020b) Diffeomorphic Smoothing for Retinotopic Mapping. In: Proceedings - International Symposium on Biomedical Imaging. IEEE Computer Society, pp 534–538

Vasseur F, Delon-Martin C, Bordier C, et al (2010) fMRI retinotopic mapping at 3 T: Benefits gained from correcting the spatial distortions due to static field inhomogeneity. J Vis 10:30–30. https://doi.org/10.1167/10.12.30

Vercauteren T, Pennec X, Perchant A, Ayache N (2009) Diffeomorphic demons: efficient non-parametric image registration. Neuroimage 45:S61–S72. https://doi.org/10.1016/j.neuroimage.2008.10.040

Wandell BA, Dumoulin SO, Brewer AA (2007) Visual field maps in human cortex. Neuron 56:366–383. https://doi.org/10.1016/j.neuron.2007.10.012

Wandell BA, Smirnakis SM (2009) Plasticity and stability of visual field maps in adult primary visual cortex. Nat Rev Neurosci 10:873–884. https://doi.org/10.1038/nrn2741

Wandell BA, Winawer J (2011) Imaging retinotopic maps in the human brain. Vision Res 51:718–737. https://doi.org/10.1016/j.visres.2010.08.004

Wang L, Mruczek REB, Arcaro MJ, Kastner S (2015) Probabilistic maps of visual topography in human cortex. Cereb Cortex 25:3911–3931. https://doi.org/10.1093/cercor/bhu277

Warnking J, Dojat M, Guérin-Dugué A, et al (2002) fMRI Retinotopic Mapping—Step by Step. Neuroimage 17:1665–1683. https://doi.org/10.1006/NIMG.2002.1304

Yeo BTT, Sabuncu MR, Vercauteren T, et al (2010) Spherical demons: Fast diffeomorphic landmark-free surface registration. IEEE Trans Med Imaging 29:650–668. https://doi.org/10.1109/TMI.2009.2030797

Zeki S, Shipp S (1988) The functional logic of cortical connections. Nature 335:311–317. https://doi.org/10.1038/335311a0

Figures

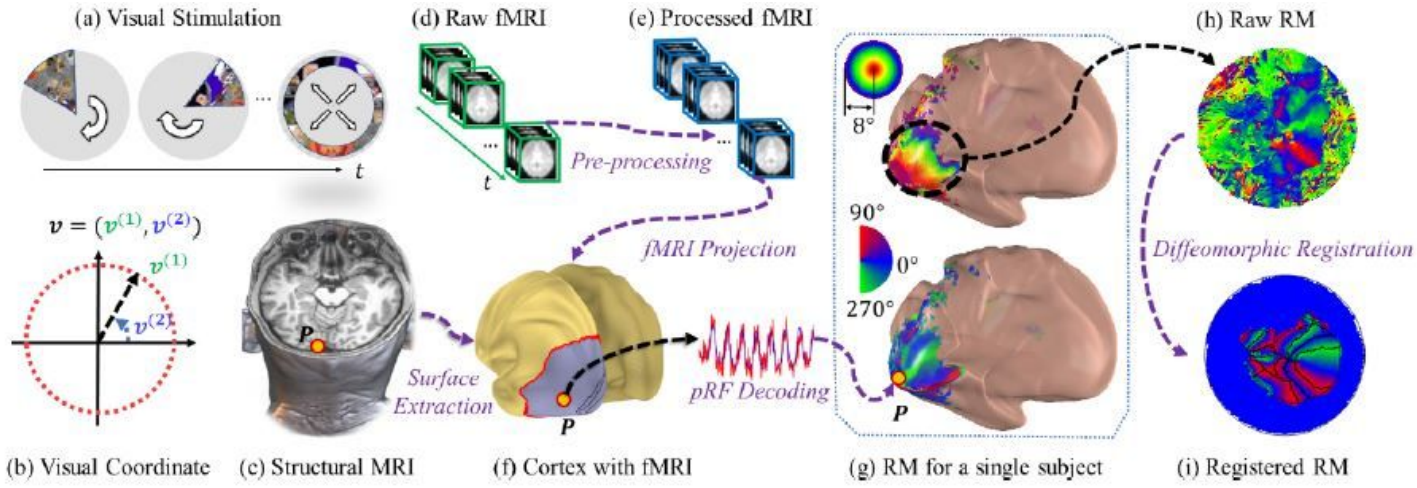

Figure 1

Illustration of a retinotopy experiment and the registration process: (a) visual stimuli, (b) the visual coordinate system, (c) structural MRI, (d) raw fMRI volumes, (e) preprocessed fMRI volumes, (f) cortical surface extracted from structural MRI with projected fMRI signals, (g) a decoded retinotopic map, (h) a raw retinotopic map projected on a flat surface, and (i) a registered retinotopic map.

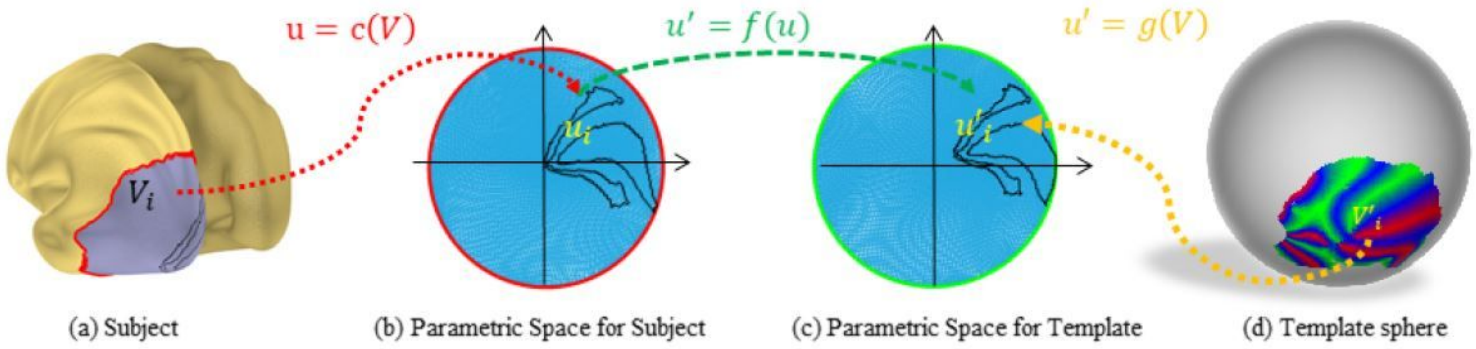

Figure 2

Illustration of several spaces and registration in the parametric space (the template sphere is rotated for illustration purpose.)

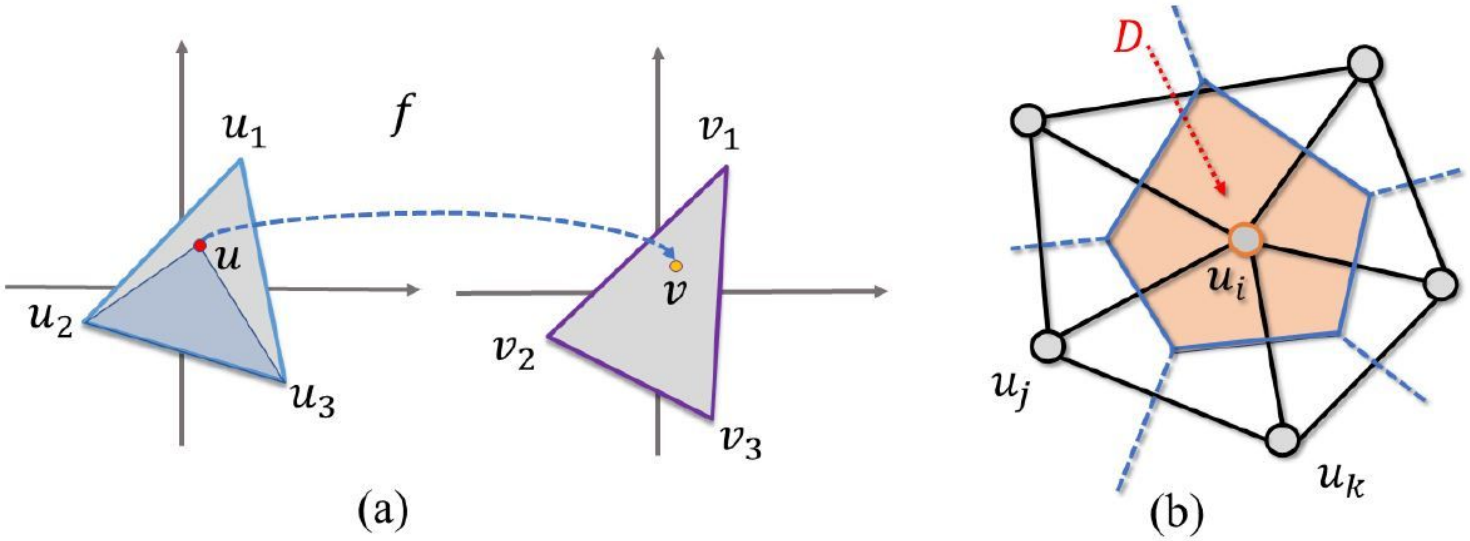

Figure 3

Illustration of a mapping function and the derivative computation. (a) an illustration of the mapping function in the discrete domain, and (b) divergence approximation for a vertex.

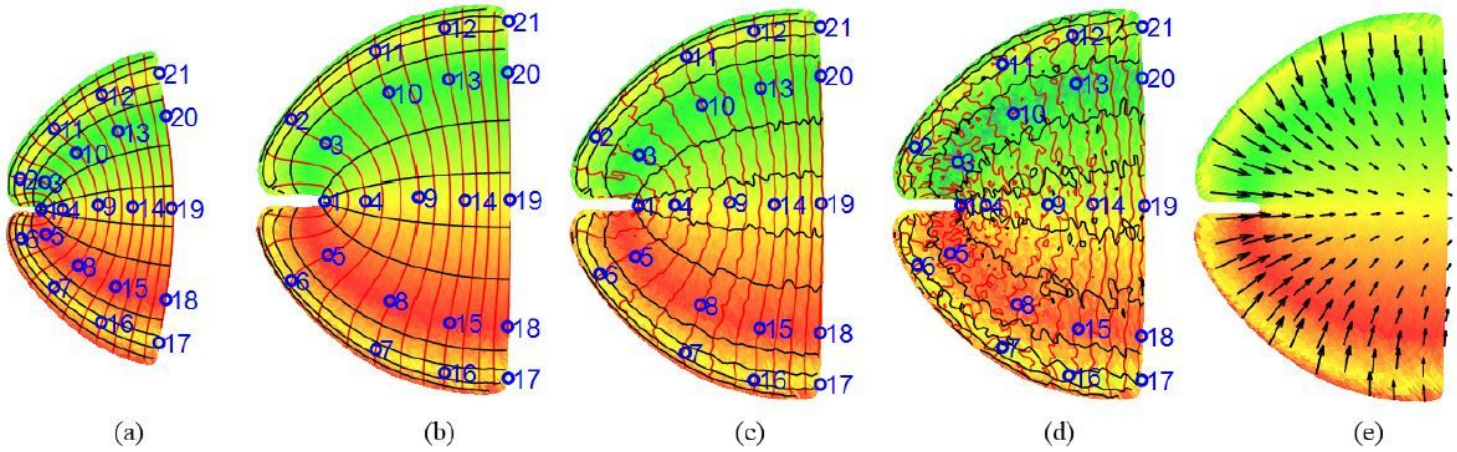

Figure 4

Template and Subject Retinotopic Maps (synthetic data): (a) The predefined template; (b) noiseless retinotopic map of a subject; (c) retinotopic map of a subject with weak noise (PSNR = 20); (d) retinotopic map of a subject with strong noise (PSNR = 10); (e) ground truth displacement. Red curves are eccentricity contours, black curves are polar angle contours, and some landmarks/anchors are marked in (a)-(d).

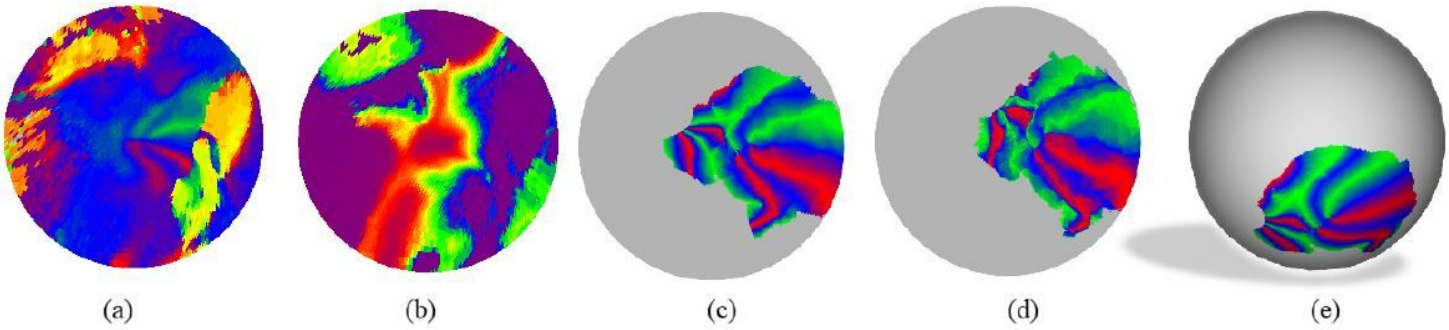

Figure 5

The Human Retinotopic Template (left hemisphere). (a) decoded polar angles of the group-average HCP retinotopic map in the disk domain; (b) decoded eccentricities of the group-average HCP retinotopic map in the disk domain, (c) BW's retinotopic model in the 2D domain, (d) the final template, (e) the template on the fsLR sphere.

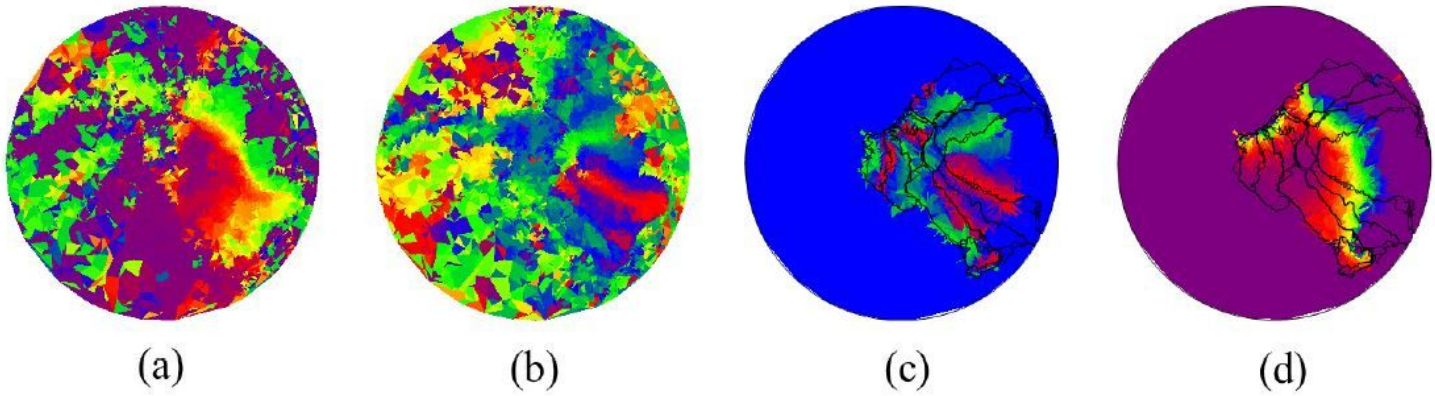

Figure 6

Before and after registration for the first observer: (a) the eccentricity of first subject, (b) polar angle of first subject, (c) registered polar angle, and (d) registered eccentricity. In (c)(d), data with eccentricity >8° are removed for clear comparation (since subjects' max eccentricity is 8°).

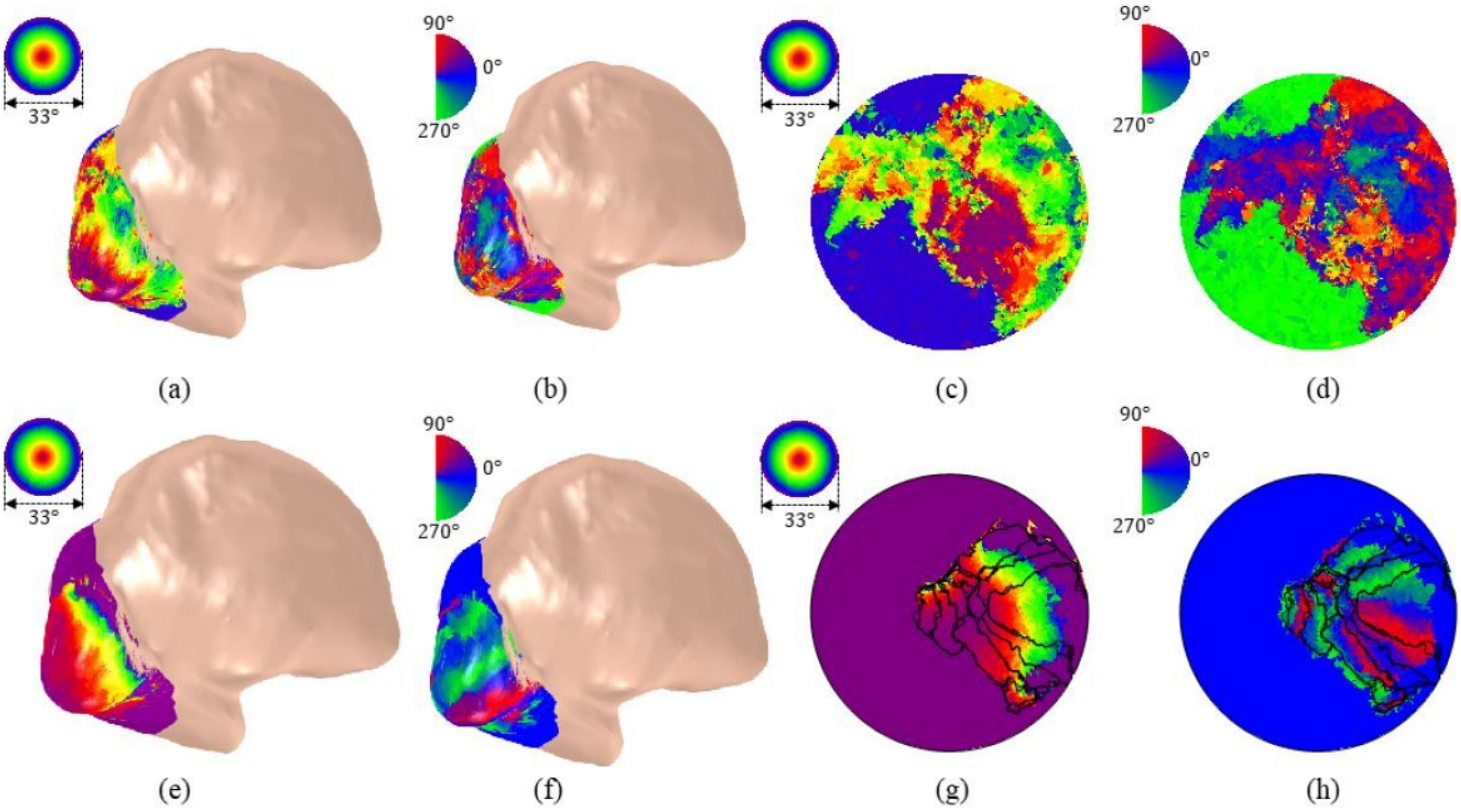

Figure 7

Retinotopic map on the left-hemisphere of the first observer in Studyforrest retinotopy dataset (Sengupta et al. 2016). (a) eccentricity map, (b) polar angle map, (c) eccentricity map on the disk, and (d) polar angle map on the disk. (e)-(h) shows the registered results correspondingly.